Springer

Effects of curing under step-by-step load on mechanical and deformation properties of cemented gangue backfill column

GUO Yu-xia(郭育霞)[1, 2], RAN Hong-yu(冉洪宇)[1, 2], FENG Guo-rui(冯国瑞)[1, 2],
DU Xian-jie(杜献杰)[1, 2], QI Ting-ye(戚庭野)[2, 3], WANG Ze-hua(王泽华)[1, 2]

1. College of Mining Engineering, Taiyuan University of Technology, Taiyuan 030024, China;
2. Shanxi Province Research Centre of Green Mining Engineering Technology, Taiyuan 030024, China;
3. Institute of Mining Technology, Taiyuan University of Technology, Taiyuan 030024, China

Abstract: A step-by-step load was utilized to mimic the load history of the backfill column in the in-situ curing process. The inner damage of the specimen during curing and uniaxial compressive testing was monitored by electrical resistivity and ultrasonic equipment. Results show that: 1) Uniaxial compressive strength (UCS) and elastic modulus (EM) of the samples curing under pressure are higher than those of the control samples without pressure, ranging in ratio from 0.5% to 20.2% and 7.1% to 52.3%, respectively, and are influenced by the initial loading age (ILA) and stress strength ratio (SSR). The SSR during curing should not exceed 80%. 2) The earlier the ILA is, the higher the total strain becomes. The higher the SSR applies, the larger the total strain gets. The creep strain increases with the increase of SSR and can be described by Burger's viscoelastic creep model. When SSR is less than 80%, the earlier the ILA is, the smaller the creep strain becomes after the last step-loading. 3) The stability of the early age backfill column under pressure can be monitored based on the change of ultrasonic pulse velocity (UPV) and electrical resistivity.

Key words: cemented gangue backfill column; curing under step-by-step load; compressive strength; elastic modulus; deformation; electrical resistivity

1 Introduction

The cemented gangue backfill material (CGBM) is a paste-like material made of coal gangue, cement, fly ash, and water [1−3]. As a type of cemented paste backfill (CPB) material, CGBM has been extensively used in backfill mining for coal resources and controlling surface subsidence. Besides, it largely reduces the accumulation of coal gangue on the surface, thus solving associated pollution issues and their impact on the ecosystem [4−8]. To minimize the cost while effectively control the surface subsidence, the partial backfill mining method has been proposed, in which the pier columns made of CGBM are used to support the roof [9−11]. Much underground space will be vacant and can be reused for other special-purpose like storage. CGBM columns distributed in the goaf are often lateral unconfined and only loaded by the vertical pressure of the roof [12−14]. Therefore, the mechanical and deformation properties of the

backfill column under vertical load are the keys to partial backfill mining [15].

A significant number of studies have conducted on the deformation and mechanical properties of CGBM and CPB. SUN et al [16, 17] studied the creep properties of CGBM under dynamic disturbance and the localized deformation properties under uniaxial compression. DU et al [12−14] discussed the failure characteristics of large unconfined backfill columns and the bearing mechanism of the cemented gangue backfill column with stirrups under the uniaxial compression test. FALL et al [18−21] studied the stress−strain behavior of CPB under the uniaxial and triaxial compression tests, and the effects of couple temperature and sulphate on strength and microstructure. CAO et al [22] investigated the structural factors (filling time, interval, and surface angle) effect on the UCS of CPB. Besides, the sulphate attack [23, 24], heat [25], and specimen size [26] have a significant influence on the mechanical properties and the pore structure of CPB. WU et al [27, 28] tested the thermal, hydraulic, and mechanical properties of CGBM, and built the thermal-hydraulic-mechanical-chemical model. XU et al [29] researched the stress−strain behavior, resistivity, and thermal infrared (TIR) characteristics of the CPB under a uniaxial compression test. The additives, such as ice [30], limestone powder, and water-reducing admixture [31−33], and loading rate [34] also influence the strength and failure properties of CPB. Except for the external influence factors, the raw material and its proportion can also affect the performance of the CGBM and CPB. QI et al [35, 36] studied the effects of fine gangue and fly ash on the strength, resistivity, and microscopic properties of CGBM. CHEN et al [37, 38] studied the effects of chloride on the early mechanical properties and microstructure of gangue-cemented paste backfill and the effects of red mud additions on gangue-cemented paste backfill properties.

Most of these studies relied on the properties of samples in a conventional curing method. However, it is not possible to ensure that all physical and mechanical properties tested from the conventional curing samples are suitable for the backfill body in the goaf [39]. Due to the continuous advancement of the coal mining face, the backfill columns at early age are loaded by the roof, and the pressure applied to the backfill column increases gradually with curing time until it tends to be stable [8]. The stability of the backfill columns at early age is essential for the continuous mining operation [15]. However, researches on the curing under pressure of early age backfill column are very limited. YILMAZ et al [40−42] discussed the effects of curing and stress conditions (simulating the self-weight pressure) on the strength, chemical, and microstructure properties of CPB. GHIRIAN et al [43] tested the strength evolution and deformation behavior of CPB under curing stress (simulate the self-weight pressure). However, the overall properties of the early age CGBM column curing under pressure of the roof are still unclear. Accordingly, a better understanding of the effects of curing under step-by-step load on mechanical and deformation properties of the CGBM column is required for a more reliable partial backfill mining design.

The purpose of this paper is to investigate the effects of curing under step-by-step load on the mechanical and deformation properties of the CGBM column. The 100 mm×100 mm×300 mm prismatic samples were curing under several step-by-step load conditions (different ILAs and different SSRs). Uniaxial compressive strength (UCS), elastic modulus (EM), and the time-dependent strain of the CGBM columns were compared. The evolution of electrical resistivity and ultrasonic pulse velocity (UPV) during curing and uniaxial compressive testing were analyzed. Besides, the relationship between UPV and UCS was established. The creep constitutive model of the early age CGBM column under step-by-step load was built. The obtained results could be used to guide the design and stability monitoring of the CGBM column in partial backfill mining.

2 Material and methods

2.1 Raw material

To satisfy the pumping performance, strength requirement, and economic benefit, the reasonable proportion range of the CGBM was obtained through a large number of experiments [12−14, 35, 36]. CGBM was mixed by ordinary Portland cement (190 kg/m^3) Type-42.5, Class F fly ash (380 kg/m^3) obtained from Xinyang Power Plant (Shanxi China), coal gangue (950 kg/m^3), tap water

(350 kg/m^3). Coal gangue was collected from Tunlan Colliery, Shanxi Province, China. After the second class cracked, it was divided into three groups (0−5 mm, 5−10 mm, 10−15 mm) according to the nominal diameter, which counted for 30%, 35%, 35% of the total coal gangue mass, respectively. The fineness module of fine aggregate (0−5 mm) was 3.10. The physical characteristics and chemical components of coal gangue, fly ash, and cement are presented in Tables 1 and 2. The particle size distribution of coal gangue is shown in Table 3. The particle size of the fly ash was shown in Ref. [36].

Table 1 Chemical components and physical properties of fly ash, and cement

Sample	$w(SiO_2)$/%	$w(Al_2O_3)$/%	$w(Fe_2O_3)$/%
Fly ash	52.42%	32.48%	3.62%
Cement	22.36%	5.53%	3.45%
Sample	$w(CaO)$/%	$w(MgO)$/%	$w(TiO_2)$/%
Fly ash	3.05%	1.01%	1.26%
Cement	65.08%	1.27%	—

Table 2 Physical properties of coal gangue, fly ash and cement

Sample	Specific gravity/ (g·cm^{-3})	Specific surface/ (m^2·kg^{-1})	Fineness (>45 μm)/%	Moisture content/%
Coal gangue	2.3	—	—	0.74
Fly ash	2.2	415	42.54	0.56
Cement	3.1	349	5	—

2.2 Preparation of CGBM sample

The preparation process of the CGBM sample is shown in Figure 1. The coarse aggregates (10−15 mm) and middle aggregates (5−10 mm) were dry mixed in a mixer for 1 min. All cement and fly

Table 3 Particle size distribution of coal gangue

Sieve size/mm	0.16	0.315	0.63	1.25
Percent of passing/%	0.95	2.20	4.41	9.65
Sieve size/mm	2.5	5	10	15
Percent of passing/%	15.14	29.78	65.24	100

ash were then added gradually into the mixer and dry mixed for 2 min. Next, the fine aggregates (0−5 mm) were added into the mixer, and mixed, then continued for another 2 min. Finally, the mixing water was added into the mixer, and the mixer was set to run for a further 3 min to produce the fresh CGBM mixture. The fresh CGBM mixture was poured into the molds with dimensions of 100 mm× 100 mm×300 mm, where two galvanized wire mesh probes at a distance of 260 mm from each end were pre-placed [44, 45]. To reduce the impact of the electrode mesh on the mechanical properties of the sample, the electrode mesh was fabricated by thin galvanized wires with a diameter of 0.8 mm and the sizes of the square hole were 15 mm×15 mm. The dimensions of the electrode mesh were 100 mm× 130 mm. All specimens were sealed and removed from the molds after casting 24 h and then placed in a standard curing room maintained at a relative humidity of 60%−80% and an ambient temperature of (24±2) °C.

2.3 Experimental setup

The experimental setup (curing under pressure apparatus) was designed to simulate in-situ different vertical pressure conditions of the roof at a laboratory scale [46, 47]. Figure 2 presents a schematic illustration of the apparatus. This apparatus can be used to assess the actual deformation and strength performance of the
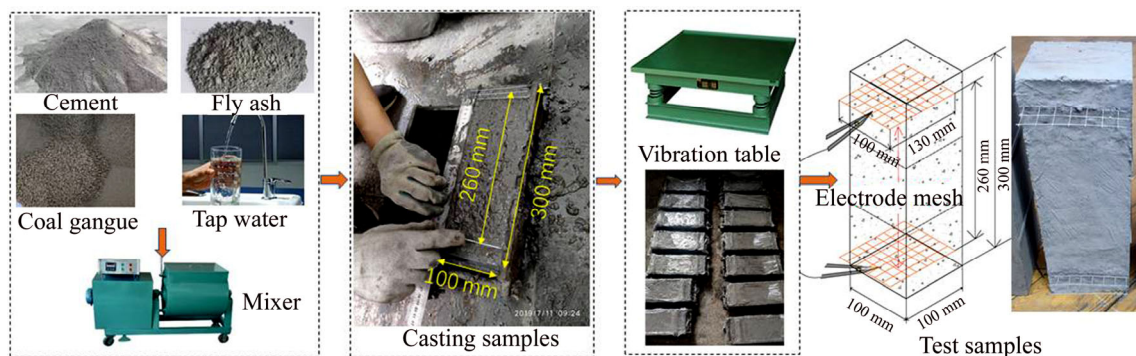

Figure 1 Specimen preparation procedures

3420

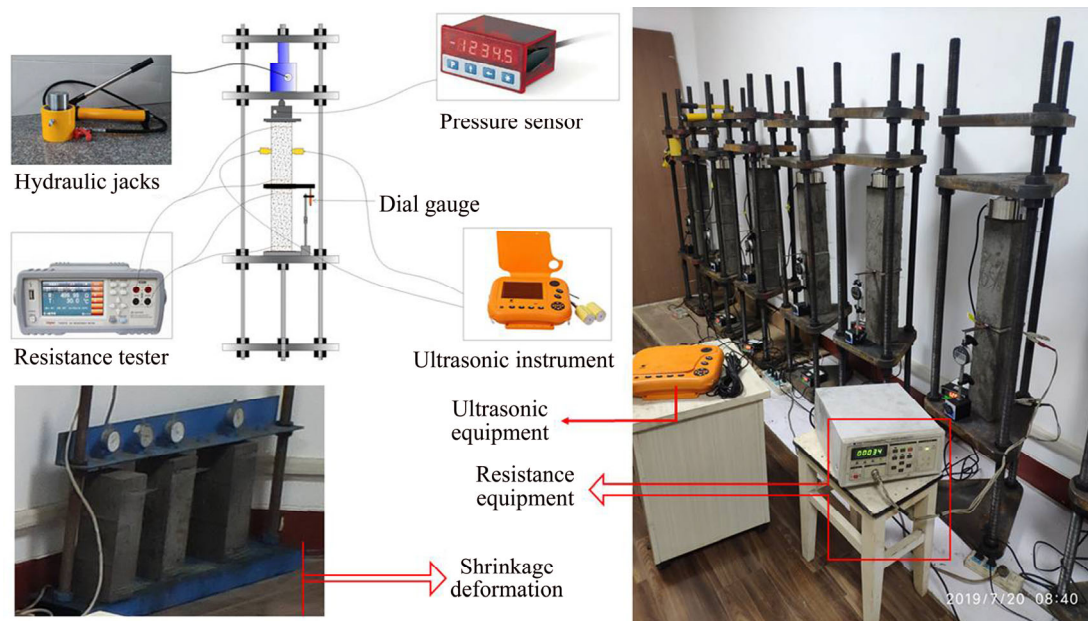J. Cent. South Univ. (2020) 27: 3417−3435

Figure 2 Schematic illustration of apparatus

CGBM sample under load by applying hydraulic pressure to the upper portion of the sample. Two specimens are in a group. The setup consists of three main components. 1) Loading system: a rigid top and bottom plate with an axial loading jack that applies a hydraulic pressure, and is equipped with a pressure sensor. The pressure is maintained within a 5% variation by adjusting the hydraulic pressure to compensate for the relaxation of the load with time. 2) Deformation monitoring system: dial gauge with 0.001 mm accuracy. 3) Inner damage evolution monitoring system: ultrasonic instrument and electrical resistance equipment are used to detect the internal damage during the curing process. The experiment was carried out at room temperature of (20±3) °C and relative humidity of 50%−60%.

2.4 Testing programs

2.4.1 Loading scheme

Figure 3(a) shows the development of UCS of CGBM samples curing under the conventional method without curing pressure. The early age CGBM columns need to bear the pressure of the roof. ZHANG et al [8] monitored the pressure development of the backfill body in the goaf that as the coal mining work-face advances continuously, the pressure applying to the backfill body increases gradually with curing time and tends to stabilize finally. Considering the different geological conditions and backfilling procedures, the initial loading time (ILA) of the roof is different, as shown

in Figures 3(b)−(d). Three ILAs, 3 d, 7 d and 14 d, were selected. According to the increasing UCS of CGBM samples cured by conventional method, six stress−strength ratios (SSR), 0, 35%, 50%, 65%, 80% and 50%-cons were chosen for each ILA. Referring to the mining process of the actual coal mine, the step-by-step loading method was adopted [47], the step-by-step loading time was set at the day 3, 7, 14 and 21. According to the design requirements of the partial backfill mining [9, 10], usually, the curing age 28 d is used to determine the uniaxial compressive strength, to make the axial strain of the CGBM sample under the pressure of the last-step loading from 21 d reaches a relatively stable state and the inner stress inside the test sample reaches the balanced state, the curing end time of 32 d was chosen.

2.4.2 Deformation monitoring

As shown in Figure 2, the axial deformation of the CGBM sample was measured on the pressure-cured samples and compared to the control samples. Axial deformation data recording commenced at the day 3, 7, 14 and continued to the day 32. Drying shrinkage data recording started from the day 3. The deformation measurement was carried out using a 20 mm demountable mechanical dial gauge with 0.001 mm accuracy. The deformation was recorded every day.

2.4.3 Electrical resistivity testing

Electrical resistivity can indirectly reflect the damages and defects, such as micro-pores and
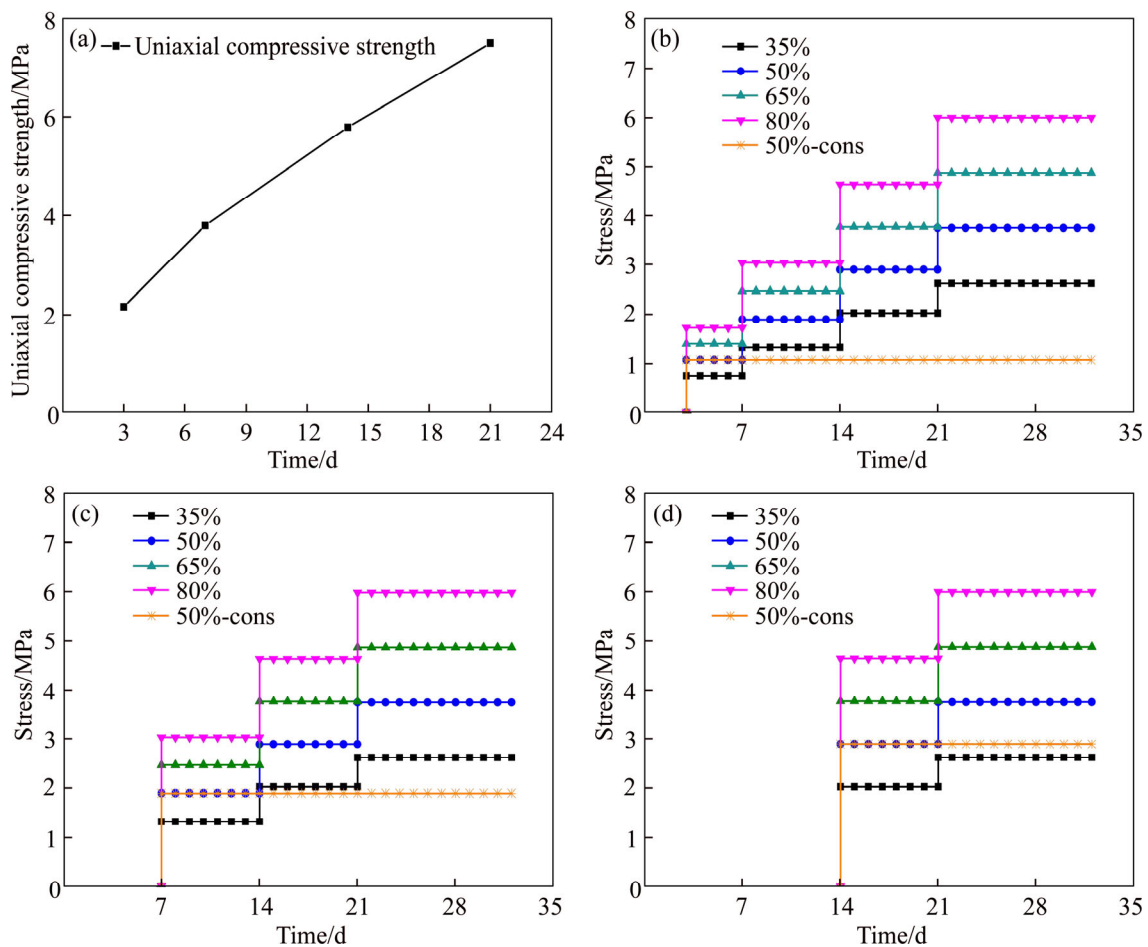
Figure 3 Pressure loading scheme of development of uniaxial compressive strength curing under conventional method without curing pressure (a), initial loading age from the day 3 (b), day 7 (c) and day 14 (d) under corresponding stress−strength ratio 35%, 50%, 65%, 80%, 50%-cons, respectively

micro-cracks [48, 49]. Once the initial electrical resistivity of the test sample is determined, the variation of electrical resistivity under loading would be mainly caused by internal damages [45]. As shown in Figure 2, the ZC2512 electrical resistance-measuring instrument was used to test the electrical resistance of the CGBM sample during the curing process. As shown in Figure 1, the electrical resistance equipment connected to two pre-embedded electrodes [44, 45], following the Kelvin four-terminal configuration and the ASTM C1760 standard [50]. The electrical resistance was recorded every day. The electrical resistance R and electrical resistivity ρ of the CGBM sample follow the equation below:

$$\rho = R \frac{S}{L} \tag{1}$$

where S is the cross-section area of the test specimen, and L is the distance between two

pre-embedded electrodes in a sample. In this experiment, the S=0.01 m^2 and L=0.26 m.

2.4.4 Ultrasonic pulse velocity testing

The EM of the CGBM sample correlated with the ultrasonic pulse wave, the damage inside the specimen has occurred after loading, which resulted in the degradation of the EM, consequently, and a change in UPV [51−53]. Therefore, as shown in Figure 2, a non-metal ultrasonic testing instrument (Model: NM-4B) was used to monitor the inner damage evolution during the curing process. The frequency of transducers was 54 kHz (40 mm diameter×50 mm length). Vaseline was applied as a coupling agent between the probes and specimen. The UPV test position was in the middle of the axial and lateral directions of the test sample (see Figure 2), and the data were tested once a day in the same position.

2.4.5 Uniaxial compression testing

When curing to 32 d, the CGBM samples were

subjected to the uniaxial compression tests described in the ASTM C39 standard for determining the UCS and EM [12]. A servo/computer-controlled testing machine (YAW-1000) with a 1000 kN loading capacity was used for the compression test. Each sample was loaded at a constant deformation rate of 0.01 mm/s. EM is the ratio of stress to strain within the elastic region of the stress−strain curve. Besides, the damage evolution during the compression process was monitored by the electrical resistance equipment and the ultrasonic instrument. All CGBM samples were prepared in the standard conditions and the mean values were presented in the results.

3 Results

3.1 Effects of curing under step-by-step load on UCS and EM

The most useful design parameters when assessing the CGBM column stability are the mechanical properties (i.e., UCS and EM) obtained from the uniaxial compression tests [40]. When CGBM specimens were cured for 32 d, the uniaxial compression test was performed. Figure 4 presents the UCS and EM of CGBM samples at different ILAs and different SSRs, and the variation of UCS and EM between the pressure-cured samples and control ones is also shown.

As shown in Figures 4(a)−(c), the UCS of all pressure-cured samples is higher than that of the control ones. For example, the difference of UCS between pressure-cured samples and control ones was 7.8%, 20.2%, 15.0%, 0.5% for ILA 3 d; 16.8%, 10.3%, 8.2%, 6.5% for ILA 7 d; and 5.6%, 13.9%, 7.7%, 5.1% for ILA 14 d. The general observation is that the variation of UCS increased first and then decreased to a lower value at a given ILA when the SSR increased from 0% to 80%. The earlier the ILA was, except the 80% SSR, the larger the increase of UCS got. The highest increase of UCS was 20.2% obtained from ILA 3 d-50%. The lowest increase of
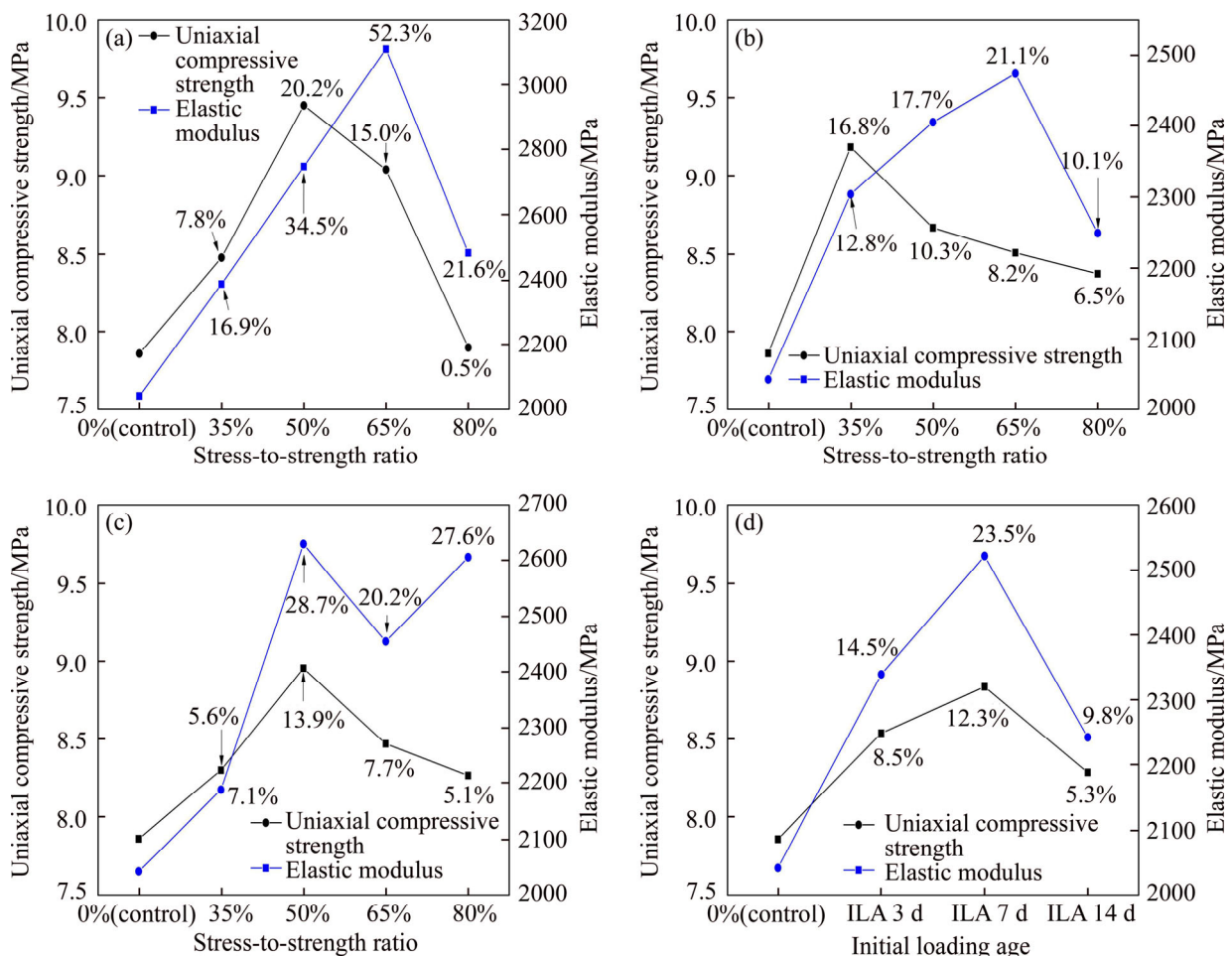

Figure 4 UCS and EM of CGBM samples at different SSRs and different ILAs ((a) 3 d, (b) 7 d, (c) 14 d); (d) UCS and EM of 50%-cons SSR at different ILA

UCS was 0.5% tested from ILA 3 d-80%. As shown in Figure 4(d), for the 50%-cons SSR samples, the growth in UCS increased from 8.5% to 12.3% and then dropped to 5.3% when ILA changed from the day 3 to day 14. Besides, the increase of UCS in the 50% SSR was higher than the 50%-cons except for ILA 7 d. It means that, at ILA 3 d and ILA 14 d, the step-by-step load contributed to the strength development of CGBM samples more than the constant pressure.

Such a variation in UCS can be associated with the cement hydration reaction. The curing pressure accelerated the cement hydration reaction, thus resulting in a denser cement matrix, which is better cohesive [40]. The micro-pores and micro-cracks of the CGBM samples are reduced by filling with the hydration products (i.e., C—S—H), hardening the strength of the CGBM sample. However, the cement bonds formed in the CGBM sample due to the cement hydration reaction may damage owing to the over-high SSR in the strength development process. Thus, the increase of UCS decreased under high SSR conditions.

Figure 4 also shows the EM of the pressure-cured samples. The EM values typically between 2.33 and 3.11 GPa for ILA 3 d, between 2.25 and 2.47 GPa for ILA 7 d, and between 2.19 and 2.63 GPa for ILA 14 d. The pressure-cured samples had respectively 16.9%, 34.5%, 52.3%, and 21.6% of ILA 3 d; 12.8%, 17.7%, 21.1%, and 10.1% of ILA 7 d; and 7.1%, 28.7%, 20.2%, 27.6% of ILA 14 d higher EM values than control samples. The most increase in EM was 52.3% at ILA 3 d-65%, and the lowest increase in EM was 7.1% at ILA 14 d-35%. The EM of the 50% SSR larger than that of the 50%-cons except for the ILA 7d. Besides, as shown in Figure 4(d), the growth of EM of the 50%-cons SSR samples increased from 14.5% to 23.5% and then dropped to 9.8% when ILA changed from 3 d to 14 d.

The porosity of a solid is inversely related to the EM [53]. Because of the curing pressure, the hydration reaction of the cement is accelerated so that the capillary porosity is reduced gradually and the stiffness of the CGBM sample is strengthened. For the ILA 3 d and ILA 7 d, the growth of EM of the 80% SSR samples has a sharp decrease, which is related to the interfacial transition zone (ITZ) between coarse aggregate and mortar. Even if the degree of cement hydration reaction has increased, some micro-cracks in ITZ cannot be repaired by the hydration products under the high SSR [54].

As shown in Figure 5, the failure pattern is different between control samples and pressure-cured ones. For the control samples (see Figure 5(a)), approximate an X-shaped conjugate slope shear failure pattern was exhibited. For the pressure-cured specimens (Figures 5(b)−(d)), a more single-slope shear failure pattern occurred, and the angle between the normal of the failure
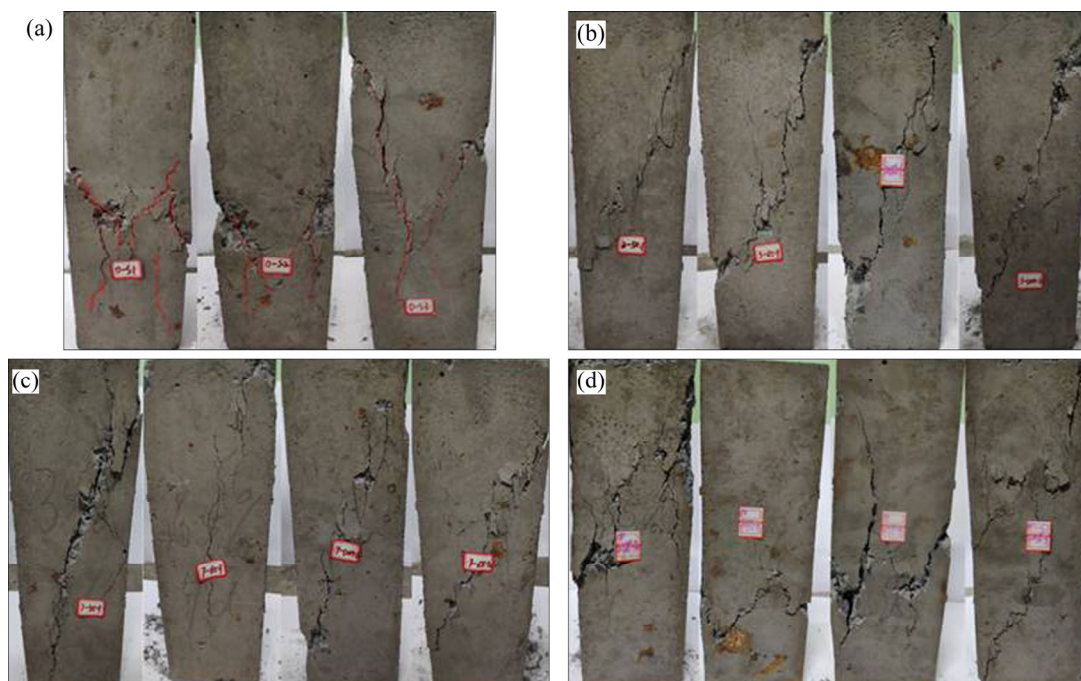

Figure 5 Failure patterns of control samples (a) and pressure-cured samples at ILA 3 d (b), 7 d (c) and 14 d (d)

surface and the loading axis was 45°−75°, and the crack penetrates the whole sample. The curing pressure affects hydration positively and the voids spaces within the CGBM's mortar are significantly reduced by filling with the fine-sized hydration products; leading to denser cementitious matrices that are reflected by a better cohesion, thereby increasing the stiffness of the CGBM column [40]. The pressure-cured samples are more compact than the control ones, and thus the shear stress of the pressure-cured samples is larger than that of the control ones. The generation and expansion of cracks are caused by the shear stress on the failure surface exceeding the limit [13]. The crack propagates along the weak face where there are more voids and microcracks in the control samples than the pressure-cured samples, which is easier to form more shear face for the control samples, finally, and the failure pattern of the control sample was X-shaped.

3.2 Shrinkage and deformation development

Figure 6(a) shows the shrinkage strain−time

curve of CGBM specimens from the 3rd day. The shrinkage strain increased from 0 to 0.0003. The speed of shrinkage increased gradually during the curing process. The shrinkage of the CGBM sample was caused by the moisture transfer from internal to the external environment. In the first few days, due to the high water-cement ratio of the CGBM sample, mainly the loss of free water in the specimens, the free water does not adhere to the microstructure of the hydration products by any physical-chemical bond [55]. Thus, the loss of free water does not accompany by apparent shrinkage. Subsequently, continuously drying leads to significant shrinkage, which mainly resulted from the loss of adsorbed water and the water held in small capillaries. The relative humidity inside the CGBM sample continuously declined as the curing age increased [46].

The step-by-step load was applied from the 3rd day, 7th day, 14th day, respectively. The resulting deformation development histories are shown in Figures 6(b)−(d). Total strain−time curves include the instantaneous elastic strain and the creep strain.
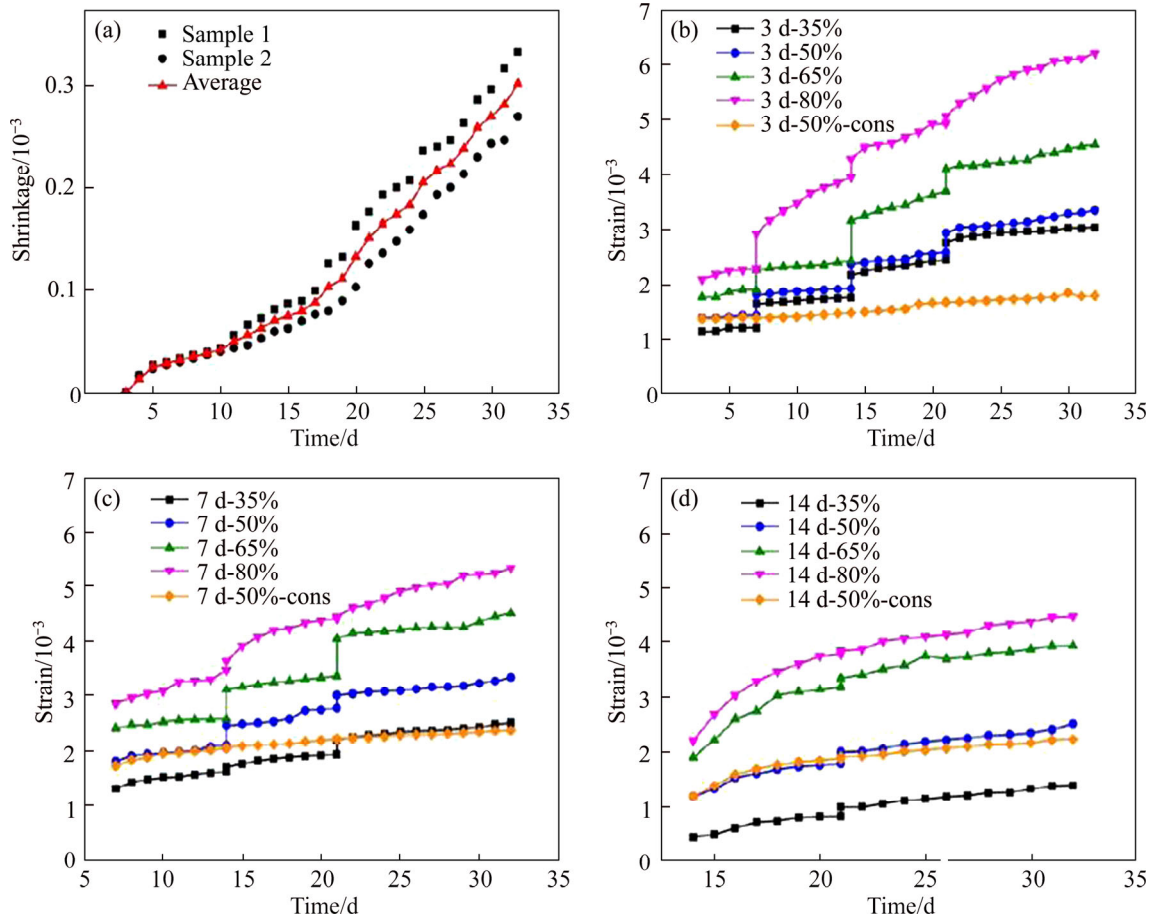

Figure 6 (a) Shrinkage strain development; The time−dependent strain of CGBM sample under step-by-step loading at different ILA, 3 d (b), 7 d (c) and 14 d (d)

The shape of the strain−time curves was similar at the same ILA, but a higher value when SSR changed from 35% to 80%. Higher SSR caused a more considerable elastic strain at a given ILA. The variation of elastic strain decreased under each subsequent step-loading. Creep strain includes two phases, i.e., decay creep and the continuously increasing steady creep. The higher the SSR applied, the larger the creep rate shown, and the more the time needed to be stable for the steady creep. Besides, the total strain of 50% SSR is higher than that of the 50%-cons. After the last step-loading, the creep rate gradually decreased with curing time. During the constant pressure phase, the micro-cracks in ITZ begin to expand, which will cause stress redistribution inside the sample, and then the stress field will reach a dynamic equilibrium [56]. Meantime, the constant curing pressure accelerates the hydration reaction of cement, and the hydration products gradually fill the micro-pores and repair some micro-cracks [41]. Therefore, the creep strain gradually tends to a constant.

Figure 7(a) further displays the total strain at different SSRs and different ILAs. The total strain increased with the increase of SSR. Besides, the earlier the ILA, the larger the total strain got at the same SSR. For example, the total strain of 3 d-80%, 7 d-80%, 14 d-80% was 0.00622, 0.00536, and 0.00448, respectively.

Figure 7(b) shows the creep strain after the last step-loading (from 21 d to 32 d) at different SSRs and different ILAs. For all the test samples, the creep strain increased with the increase of SSR. At the same SSR, except for the 80% SSR, the earlier the ILA, the smaller the creep strain. It means that

when SSR was smaller than 80%, the early loading history decreased the creep strain after the last step-loading. However, for the 80% SSR, the creep strain decreased with the increase of the ILA. When the ILA was 3 d or 7 d, micro-cracks due to high SSR are easier to form in the CGBM column. The stiffness of the CGBM column will be weakened when inner damage occurs, resulting in more micro-cracks. With the increase of constant pressure, these micro-cracks expanded gradually during the creep process after the last step-loading, which will cause larger creep strain.

3.3 Electrical resistivity properties during curing process

Figure 8 details the evolution of the electrical resistivity of both control and pressure-cured samples during the curing process. For the control samples curing from 3 d to 32 d (Figure 8(a)), the electrical resistivity decreased from 6.79 to 0.22 kΩ·m first and then increased to 6.64 kΩ·m gradually [30, 50]. Before 7 d, the free water in the sample reduced continuously due to the consumption of cement hydration reaction and transfer to the external environment. The ion concentration in the micro-pores increased so that the electrical resistivity declined. After that, the continuous cement hydration reaction produced more hydration products, which resulted in the growth of electrical resistivity [50].

When ILA was 3 d (Figure 8(b)), the electrical resistivity of the pressure-cured samples (SSR 35%, 65%, 80%) decreased from 3 d to 7 d first and then increased continuously, and the electrical resistivity of the pressure-cured sample was higher than that of the control sample. For the 50% SSR, the lowest
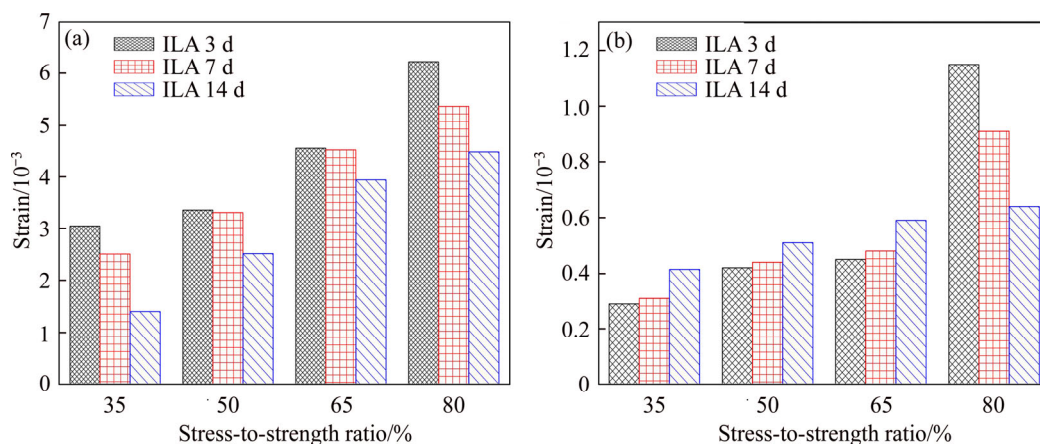

Figure 7 (a) Total strain of pressure-cured samples under step-by-step loading; (b) Creep strain after the last step-loading (from 21 d to 32 d)
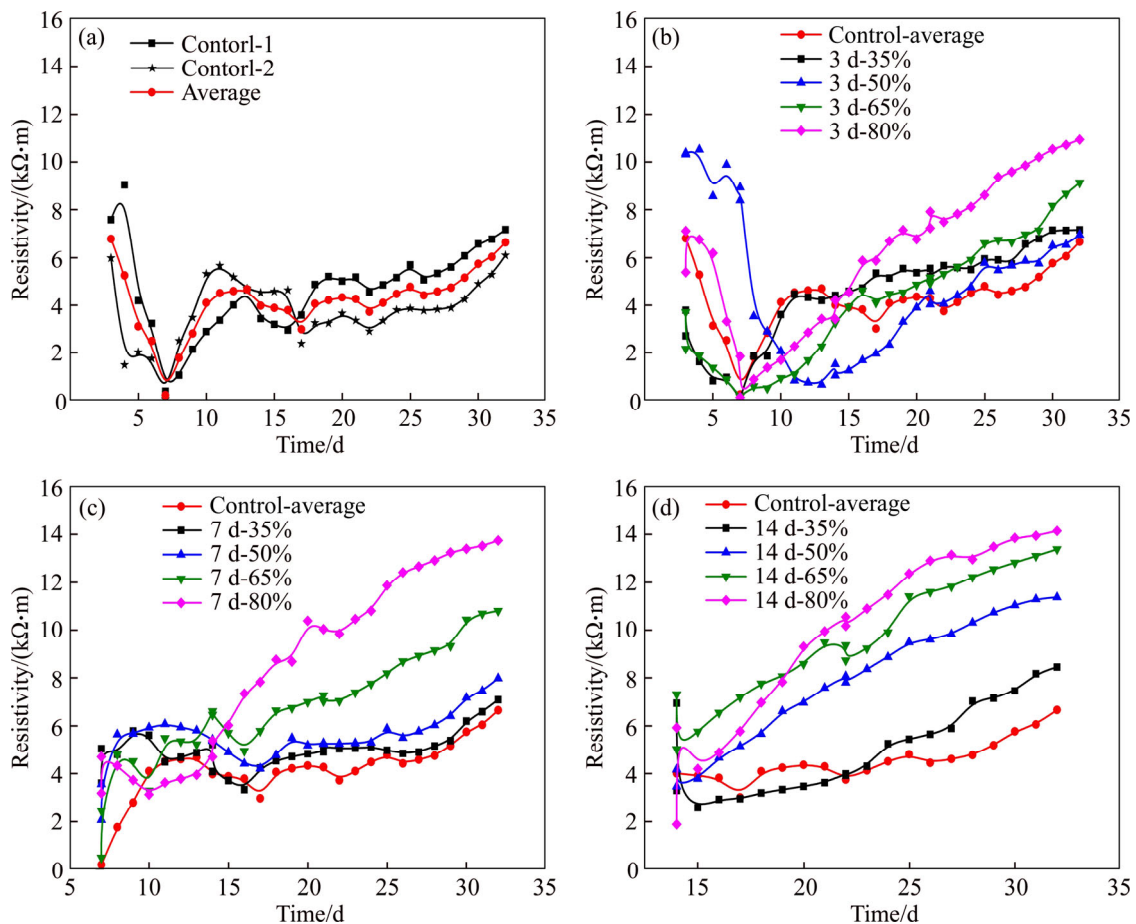
Figure 8 Evolution of electrical resistivity during curing process: (a) Control samples; (b−d) Pressured samples at ILA, 3 d, 7 d, 14 d, respectively

electrical resistivity occurred at the 12th day. When ILA was 7 d (Figure 8(c)), for all the pressure-cured samples (SSR 35%, 50%, 65% and 80%), electrical resistivity increased with the increasing of curing time. Besides, the higher the SSR was, the larger the increase rate of electrical resistivity became. When ILA was 14 d (Figure 8(d)), the electrical resistivity of all the samples except for the 80% SSR decreased after the initial loading. The electrical resistivity of the 80% SSR increased sharply when the first step-load was applied to the specimen. Subsequently, the electrical resistivity of all the samples increased with the curing time, and the growth rate of electrical resistivity increased with the increase of SSR.

Overall, before the curing age 7 d, ion concentration in the capillary pore is the main effect factor on the variation of electrical resistivity. However, after 7 d, the hydration products and the micro-cracks under the curing pressure are the most critical effect factors on the change of electrical resistivity. The higher the SSR was, the more the

hydration products and cracks produced in the CGBM sample are. Thus, the higher the increase rate of electrical resistivity will be.

3.4 Ultrasonic pulse velocity properties during curing process

Figure 9 shows the variation of UPV with curing time under different ILAs and different SSRs. For the control samples (Figure 9(a)), the UPV approximated linearly increased at first and then gradually tended to be stable [53, 57]. For all the pressure-cured samples (Figures 9(b)−(d)), the shape of the UPV-time curves at different SSRs was similar to that of the control sample. The UPV suddenly decreased when the first step-load was applied to the CGBM samples. The higher the SSR was, the larger the amplitude of decline, and then the UPV continuously increased until it tended to be stable. Except for the 80%-SSR group, the UPV of all the pressure-cured samples was higher than that of the control group. The highest final UPV was 2.75 km/s at ILA 7d-35% SSR. The lowest final
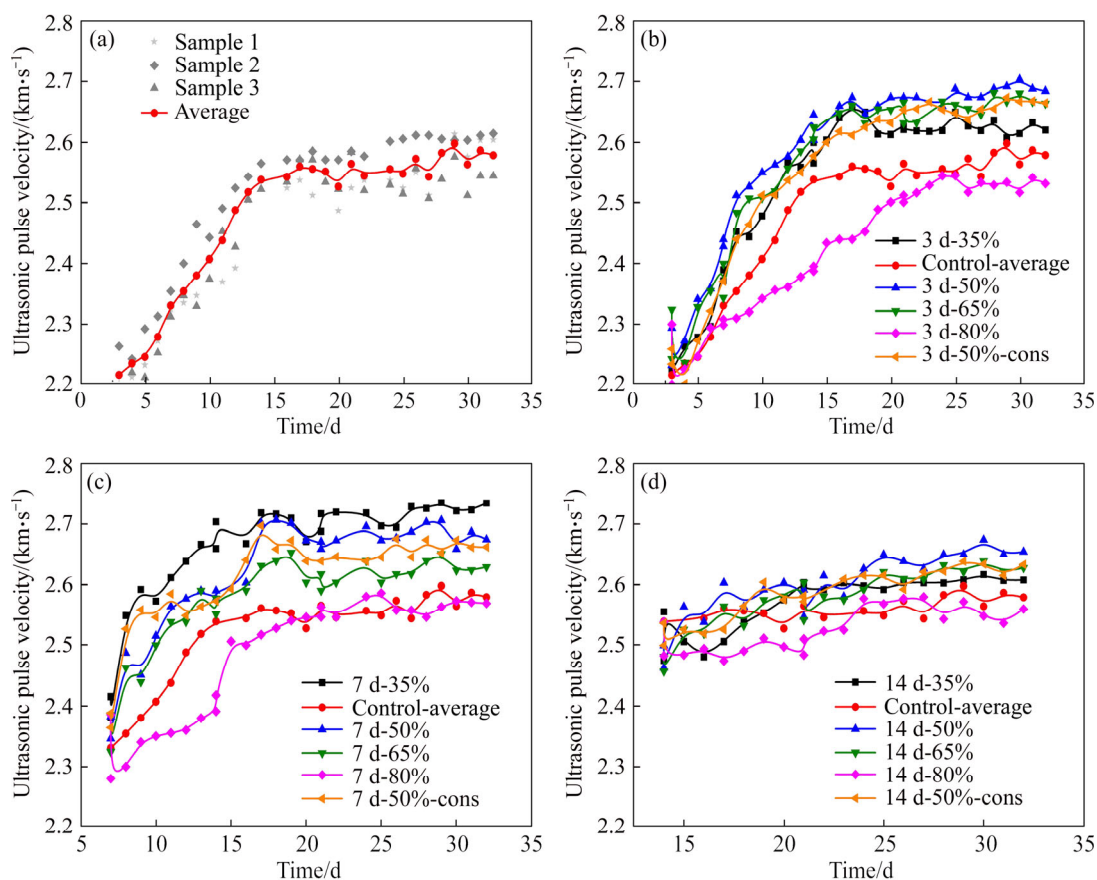
Figure 9 Evolution of UPV during the curing process: (a) Control samples; (b−d) Pressure-cured samples at ILA 3 d, 7 d, 14 d, respectively

UPV was 2.52 km/s at ILA 3d-80% SSR.

As shown in Figures 9(b)−(d), except for the 80% SSR samples, the UPV growth rate of the pressure-cured sample was higher than that of the control ones. It means that the curing pressure promotes the hydration reaction of cement during the curing process. The cement hydration products filled the micro-pores and repaired the micro-cracks, which increased the compactness of the CGBM column. However, for the 80% SSR samples, the UPV growth rate smaller than the control sample is probably due to the micro-cracks in ITZ.

What's more, the value of UPV corresponds to the applied SSR. For the ILA 3 d (Figure 9(b)), the 50% SSR had the highest final UPV, followed by 65% and 35%; the UPV of the 80% SSR samples was lower than that of the control samples. It can be considered that high SSR causes new cracks in the ITZ. The ultrasonic pulse travels around these cracks, which would increase the transit time of the pulse and reduce the UPV [53, 57]. For the ILA 7 d (Figure 9(c)), the 35% SSR had the highest final UPV, followed by 50% and 65%. The UPV of the

80% SSR before 18d was lower than that of the control samples, but it gradually increased to the control sample's level due to the continuous cement hydration. When the ILA was 14 d (Figure 9(d)), the 50% SSR had the highest final UPV, followed by 65% and 35%. The increase in UPV of the pressure-cured specimens was greater than that of the control ones. The UPV of ILA 14 d was smaller than that of the ILA 3 d and ILA 7 d at the same SSR. It means that the later the ILA, the less the new corresponding hydration products generated under the curing pressure. The UPV of all the 50%-cons SSR samples was lower than that of the 50% SSR. It means that the step-by-step curing pressure can promote the cement hydration reaction better.

4 Discussion

4.1 Bearing capacity improvement under curing pressure

During the CGBM column casting process, bleeding behavior is inevitable around the coarse

aggregate [58]. A layer of water film will form under the coarse aggregate, which increases the water-cement ratio, and the crystalline products around the coarse aggregate are coarser crystals (Figure 10(a)). The ITZ is prone to cracking when subject to tensile stress caused by differential movement between aggregate and mortar, such as CGBM in a dry environment [56]. Cracks can occur at the 30% SSR in the ITZ [59]. These cracks can be present to develop further when a load is applied and sustained [53]. Besides, the high water-cement ratio of CGBM results in the high porosity in the mortar, which is easy to produce cracks under the load.
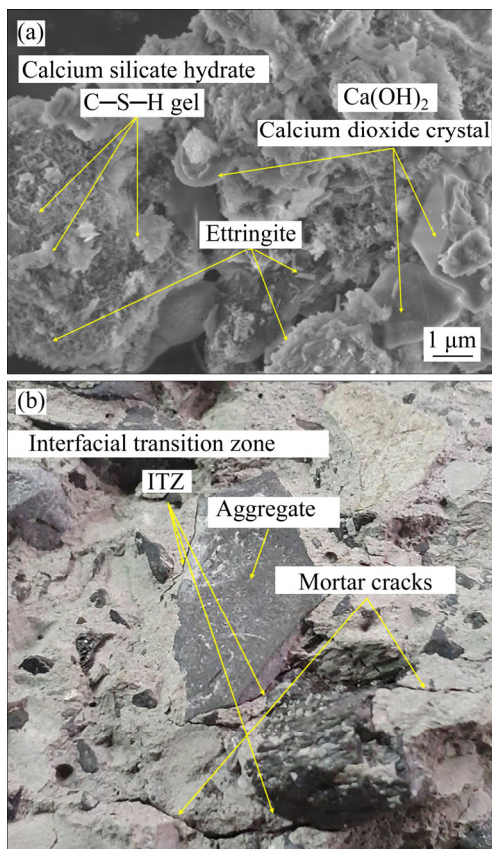

Figure 10 SEM images of hydration products in ITZ (a) and cracks in both ITZ and mortar (b)

Although there are many negative factors to the bearing capacity for the CGBM column, the UCS and EM of pressure-cured samples are still higher than that of the control ones. The early age CGBM column has a strong self-healing ability for its micro-cracks under the curing stress [54]. Due to the curing stress, part of the micro-cracks will be closed in the ITZ. Meantime, the unhydrated cement particles tend to agglomerate, forming a flocculated structure to enclose a large amount of

mixing water. Under constant load, the pore water pressure increases, which accelerates the cement hydration reaction with the mixing water. A large number of hydration products are produced (mainly C—S—H), which increases cohesion and repairs micro-cracks in the ITZ [40]. Besides, the newly formed large amount of C—S—H gels fill the micro-pores and repair the micro-cracks in the mortar [41, 60]. Thus, the porosity is reduced [61, 62], and the UPV of the pressure-cured samples is higher than that of the control ones (Figure 9). If appropriate measures are taken to control the ILA and the SSR of the roof, the UCS and EM of the CGBM column can be increased by 1.202 times and 1.523 times, respectively. It is meaningful for the long-term stability of the CGBM column in partial backfill mining.

Although the strength of the 80% SSR samples is slightly larger than that of the control ones, the electrical resistivity rises sharply, and the UPV of pressure-cured samples is lower than that of the control ones (see Figures 8 and 9), which means that curing pressure also will cause damages inside of the backfill column. New cracks are produced in both ITZ and mortar under the high curing pressure. The high curing pressure accelerates the cement hydration reaction, but part of the cracks in ITZ cannot be repaired by the hydration products [54]. With the increase of pressure, the stress concentration of the macropores in the mortar is enough to cause cracks, and these cracks gradually expand until the primary cracks in ITZ are connected (see Figure 10(b)). These macro-cracks will quickly develop and propagate, and the backfill column will suddenly destroy. Therefore, the pressure of the roof applied to the early age CGBM column should not exceed 80% SSR.

4.2 Creep constitutive model under step-by-step loading

As shown in Figure 6, the strain−time curves of the CGBM column after each step-loading include two stages, the instantaneous elastic strain, followed by a creep stage. The creep strain is comprised of the transient and steady creep stage. The creep rate decreased gradually toward a constant value. Creep strain is often modeled by rheological equations. Burger's viscoelastic model is often used to describe the creep behavior of soft rock [63]. The model is a series of Maxwell model

and Kelvin model, which was presented by the following constitutive equation [16]:

$$\varepsilon(t)= \frac{\sigma}{E_\mathrm{M}} + \frac{\sigma}{\eta_\mathrm{M}} t + \frac{\sigma}{E_\mathrm{K}} \left(1 - e^{-\frac{E_\mathrm{K}}{\eta_\mathrm{K}}} \right) \qquad (2)$$

where $\varepsilon(t)$ is the creep strain calculated at a loading time t; σ is the stress applied to the CGBM samples; E_M and η_M are the elastic parameter and viscosity coefficient of the Maxwell model, respectively; E_K and η_K are the elastic parameter and viscosity coefficient of the Kelvin model, respectively.

Take the CGBM samples of ILA 7 d as examples. Burger's constitutive model parameters are fitted, and the fitting results are shown in Table 4. The obtained fitting results are substituted into the creep equation for calculation, and the calculated results are compared with the experimental data, as presented in Figure 11. Two groups of results show a high degree of coincidence. Therefore, Burger's constitutive equation can appropriately express the creep strain of the early age CGBM column under the step-by-step load of the roof.

4.3 Relationship between UPV and UCS

Figure 12 shows the relationship between final UPV and UCS when SSR increases from 35% to 80% at different ILAs. The final UPV versus UCS shows an exponential relationship. The UCS increased with the increasing of UPV. When SSR is ranging in 35%−65%, CGBM samples are loaded in the elastic phase. UPV is mainly affected by the continuously generated hydration products. When the SSR is 80%, the CGBM samples are loaded in the plastic stage. UPV is primarily influenced by internal cracks [45]. Thus, the UCS and UPV of the 80% SSR samples are the lowest.

4.4 Stability monitoring of cemented gangue backfill column

The damage of the CGBM column is closely related to the internal cracks. As shown in Figures 8 and 9, the damage of the CGBM column curing under pressure corresponded to the variation of electrical resistivity and UPV, and was influenced by the ILA and SSR. When the internal damage of the CGBM column increases, the electrical resistivity increases, and the UPV decreases.

Besides, as shown in Figure 13, the variations of electrical resistivity and UPV under the uniaxial compressive tests are corresponding to the stress−strain curve. The failure of the CGBM column has two stages, the compaction stage, and the crack generation and expansion stage [13]. Electrical resistivity decreased gradually because of the compaction of the pores and micro-cracks, and then electrical resistivity increased quickly with the cracks generated and extended. Finally, electrical resistivity increased to a relatively high point, and the test sample was in failure. The variation of electrical resistivity before the peak-stress is influenced by the failure pattern [44]. It needs more experiments to determine the accurate change curve of electrical resistivity at different failure patterns in

Table 4 Parameter fitting results

| Stress-to-strength ratio	Stress/MPa	E_M/MPa	η_M/(MPa·d)	E_K/MPa	η_K/(MPa·d)	R-square
	1.33	1016.892	46486.011	11075.254	7214.065	0.995
35%	2.03	1188.019	1.58114E8	7623.452	27295.971	0.995
	2.625	1194.502	115465.250	61264.912	41071.374	0.975
	1.90	1050.012	56985.250	34014.853	14828.977	0.964
50%	2.90	1194.892	58558.013	9.516E8	33745.219	0.954
	3.75	1241.768	179870.041	1.161E9	15731.959	0.942
	2.47	1024.765	1.70793E9	12030.232	43234.209	0.999
65%	3.77	1212.440	136854.178	65418.380	118724.550	0.999
	4.875	1207.779	129779.818	295181.918	16004.033	0.981
	3.04	1066.633	38417.434	118233.941	2366.057	0.948
80%	4.64	1278.687	104390.219	9532.649	14844.260	0.994
	6.00	1347.131	125977.144	15062.196	64385.001	0.987
50%-cons	1.90	1087.683	116525.325	8269.283	28268.839	0.995
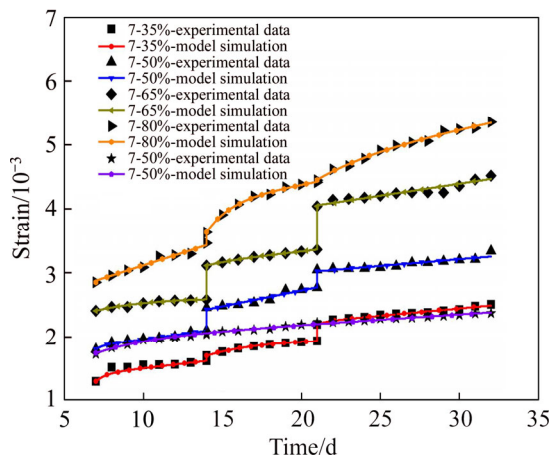
Figure 11 Comparison of simulation and experimental results of the ILA 7d

the next work. During the compacting process, no macro-cracks are formed in the CGBM sample. The UPV fluctuates continuously [12]. When the stress reaches the peak stress, UPV suddenly drops due to the macro-cracks generated in the sample. In the post-peak phase, UPV decreases continually until the test sample destroys utterly.

The UPV and electrical resistivity have an inflection point near the peak of the stress−strain curve, which can be regarded as the instability feature point of the backfill column in the goaf. Therefore, pre-embedding the ultrasonic probe inside the backfill column [64], combined with the variation of electrical resistivity between the two electrode meshes [44, 45], it is possible to achieve the stability monitoring of the early age CGBM column under the pressure of the roof in partial backfill mining.

5 Conclusions

1) Curing under step-by-step load to mimic the in-situ early age backfill column stress conditions increases the UCS and EM of CGBM samples. The curing pressure contributed positively to the cement hydration reaction process. The UCS and EM of pressure-cured samples were 0.5% to 20.2% and 7.1% to 52.3% higher than the control ones, respectively. The UCS and EM of pressured-cured samples were influenced by ILA and SSR. The pressure applied to the backfill column should not exceed the 80% SSR during the curing process in practical partial backfill mining. Otherwise, cracks will occur inside the backfill column, even cause
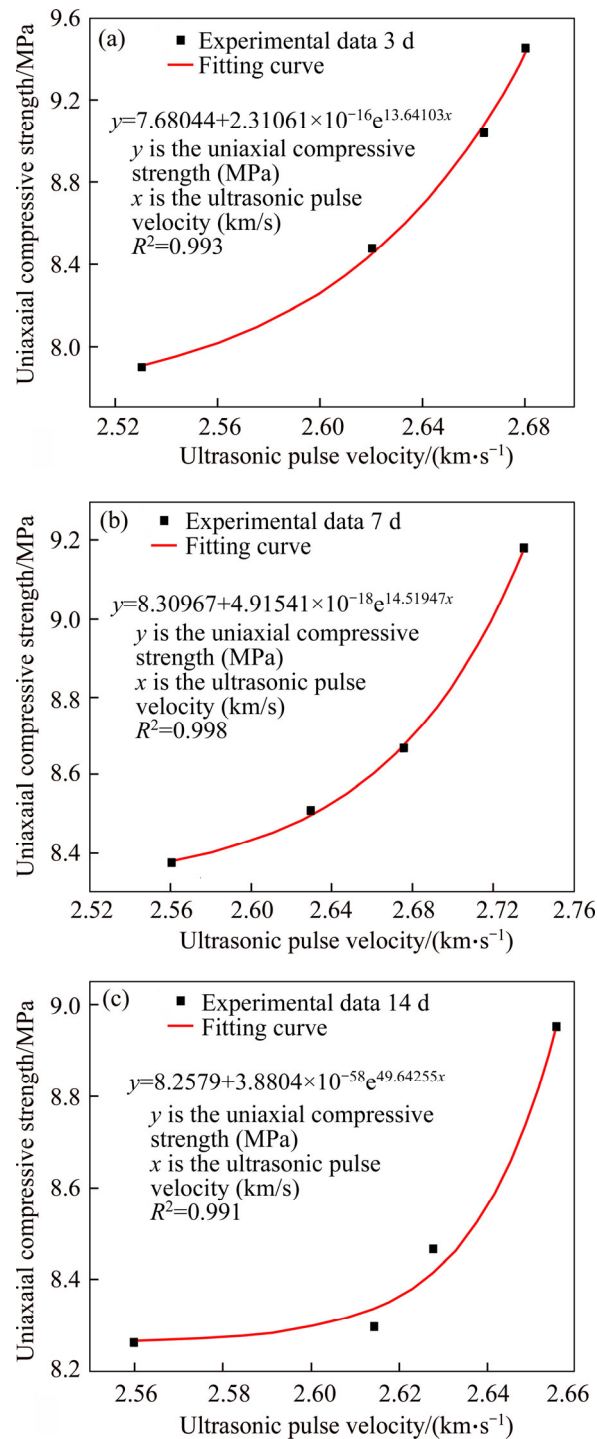

Figure 12 Relationship between final UPV and UCS: (a) ILA 3 d; (b) ILA 7 d; (**c**) ILA 14 d

instability of the backfill column.

2) The earlier the ILA is, the higher the total strain becomes at the same SSR. The higher the SSR applies, the larger the total strain gets at the same ILA. The creep strain increases with the increase of SSR. The creep rate decreases with the increase of curing time. The early loading history has an impact on the creep strain after the last
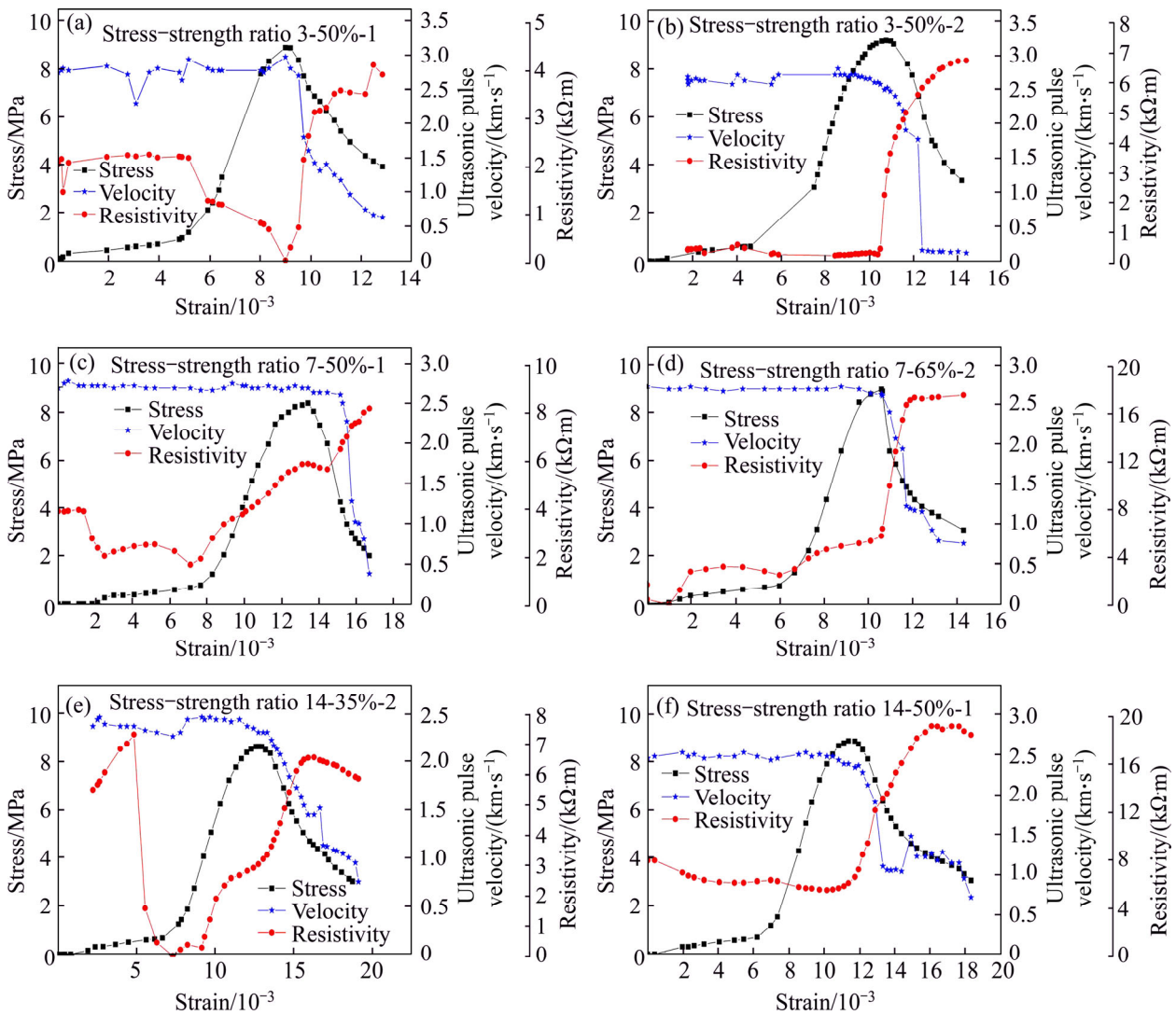
Figure 13 Relationship between electrical resistivity, UPV, and stress−strain curve under uniaxial compression test: (a, b) ILA 3 d; (c, d) ILA 7 d; (e, f) ILA 14 d

step-loading. When SSR is less than 80%, the earlier the ILA is, the smaller the creep strain becomes after the last step-loading. For the 80% SSR, the earlier the ILA is, the higher the creep strain becomes after the last step-loading. The creep strain of the CGBM column at early age under step-by-step loading can be described by Burger's viscoelastic model.

3) UPV increases with the increasing of curing time and gradually tends to stabilize. The UPV and the growth rate of UPV of the pressure-cured samples except for the 80% SSR are higher than that of the control ones. Final UPV and UCS show an exponential relationship when SSR increased from 35% to 80%. Electrical resistivity decreased with the increasing of curing time before 7 d and then gradually increased. The higher the applied

SSR is, the higher the growth rate of electrical resistivity will be. The variation of UPV and electrical resistivity shows a corresponding relationship with the stress−strain curve of the CGBM sample under uniaxial compressive tests.

The pressure-cured samples can be used to evaluate in-situ CGBM column mechanical and deformation behavior better. The experimental results could be used to guide the design and stability monitoring of the CGBM column in partial backfill mining.

Contributors

The overarching research goals were developed by GUO Yu-xia, FENG Guo-rui and RAN Hong-yu. RAN Hong-yu and GUO Yu-xia did the experiment and the analyzed the experimental

data. The initial draft of the manuscript was written by GUO Yu-xia and RAN Hong-yu. FENG Guo-rui, DU Xian-jie, QI Ting-ye and WANG Ze-hua revised the original manuscript. All authors replied to reviewers' comments and revised the final version.

Conflict of interest

GUO Yu-xia, RAN Hong-yu, FENG Guo-rui, DU Xian-jie, QI Ting-ye and WANG Ze-hua declare that they have no conflict of interest.

References

[1] ZHANG Qin-li, WANG Xin-min. Performance of cemented coal gangue backfill [J]. Journal of Central South University of Technology, 2007, 14(2): 216−219. DOI: 10.1007/s11771-007-0043-y.

[2] WU Di, YANG Bao-gui, LIU Yu-cheng. Pressure drop in loop pipe flow of fresh cemented coal gangue-fly ash slurry: Experiment and simulation [J]. Advanced Powder Technology, 2015, 26(3): 920−927. DOI: 10.1016/j.apt.2015.03.009.

[3] WU D, ZHANG Y, WANG C. Modeling the thermal response of hydrating cemented gangue backfill with admixture of fly ash [J]. Thermochimica Acta, 2016, 623: 86−94. DOI: 10.1016/j.tca.2015.11.007.

[4] BENZAAZOUA M, OUELLET J, SERVANT S, NEWMAN P, VERBURG R. Cementitious backfill with high sulfur content physical, chemical, and mineralogical characterization [J]. Cement and Concrete Research, 1999, 29(5): 719−725. DOI: 10.1016/ S0008-8846(99)00023-X.

[5] BENZAAZOUA M, FALL M, BELEM T. A contribution to understanding the hardening process of cemented pastefill [J]. Minerals Engineering, 2004, 17(2): 141−152. DOI: 10.1016/j.mineng.2003.10.022.

[6] YILMAZ E. Advances in reducing large volumes of environmentally harmful mine waste rocks and tailings [J]. Gospodarka Surowcami Mineralnymi-Mineral Resources Managemen, 2011, 27: 89−112. DOI: 10.1016/j.ijrmms.2010.08.005.

[7] YAO Yuan, SUN Heng-hu. A novel silica alumina-based backfill material composed of coal refuse and fly ash [J]. Journal of Hazardous Materials, 2012, 213−214: 71−82. DOI: 10.1016/ j.jhazmat.2012.01.059.

[8] ZHANG Xin-guo, LIN Jia, LIU Jin-xiao, LI Fei, PANG Zhen-zhong. Investigation of hydraulic-mechanical properties of paste backfill containing coal gangue-fly ash and its application in an underground coal mine [J]. Energies, 2017, 10(9): 1309. DOI: 10.3390/en10091309.

[9] FENG Guo-rui, DU Xian-jie, GUO Yu-xia, QI Ting-ye, WANG Ze-hua, LI Qing-dong, LI Hua-yun, KANG Li-xun. Basic theory of constructional backfill mining and the underground space utilization concept [J]. Journal of China Coal Society, 2019, 44(1): 74−84. DOI: 10.13225/j.cnki.jccs.2018.1598. (in Chinese)

[10] XIE Jian-lin, ZHU Wei-bing, XU Jia-lin, WEN Jia-hui, LIU Chuan-zhen. A study on the bearing effect of pier column backfilling in the goaf of a thin coal seam [J]. Geosciences Journal, 2016, 20(3): 361−369. DOI: 10.1007/s12303-015-0047-9.

[11] ZHU Wei-bing, XU Jing-min, XU Jia-lin, CHEN Da-yong, SHI Jian-xin. Pier-column backfill mining technology for controlling surface subsidence [J]. International Journal of Rock Mechanics and Mining Sciences, 2017, 96: 58−65. DOI: 10.1016/j.ijrmms.2017. 04.014.

[12] DU Xian-jie, FENG Guo-rui, GUO Yu-xia, QI Ting-ye, ZHANG Yu-jiang, GUO Jun. Failure analyses of unconfined CCWBM body in uniaxial compression based on central pressure variation [J]. Waste Management & Research, 2018, 36(2): 159−168. DOI: 10.1177/07342 42X17748365.

[13] DU Xian-jie, FENG Guo-rui, QI Ting-ye, GUO Yu-xia, ZHANG Yu-jiang, WANG Ze-hua. Failure characteristics of large unconfined cemented gangue backfill structure in partial backfill mining [J]. Construction and Building Materials, 2019, 194: 257−265. DOI: 10.1016/j.conbuildmat. 2018.11. 038.

[14] DU Xian-jie, FENG Guo-rui, ZHANG Yu-jiang, WANG Ze-hua, GUO Yu-xia, QI Ting-ye. Bearing mechanism and stability monitoring of cemented gangue backfill column with stirrups in partial backfill engineering [J]. Engineering Structures, 2019, 188: 603−612. DOI: 10.1016/j.engstruct. 2019.03.061.

[15] POKHAREL M, FALL M. Coupled thermochemical effects on the strength development of slag-paste backfill materials [J]. Journal of Materials in Civil Engineering, 2010, 23(5): 511−525. DOI: 10.1061/(asce)mt.1943-5533.0000192.

[16] SUN Qi, LI Bing, TIAN Shuo, CAI Chang, XIA Ya-jie. Creep properties of geopolymer cemented coal gangue backfill under dynamic disturbance [J]. Construction and Building Materials, 2018, 191: 644−654. DOI: 10.1016/j.conbuildmat.2018.10.055.

[17] SUN Qi, CAI Chang, ZHANG Shu-kun, TIAN Shuo, LI Bing, XIA Ya-jie, SUN Qing-wei. Study of localized deformation in geopolymer cemented coal gangue backfill based on the digital speckle correlation method [J]. Construction and Building Materials, 2019, 215: 321−331. DOI: 10.1016/j.conbuildmat.2019.04.208.

[18] FALL M, BELEM T, SAMB S, BENZAAZOUA M. Experimental characterization of the stress–strain behaviour of cemented paste backfill in compression [J]. Journal of Materials Science, 2007, 42(11): 3914−3922. DOI: 10.1007/ s10853- 006-0403-2.

[19] FALL M, CÉLESTIN J C, POKHAREL M, TOURÉ M. A contribution to understanding the effects of curing temperature on the mechanical properties of mine cemented tailings backfill [J]. Engineering Geology, 2010, 114(3, 4): 397−413. DOI: 10.1016/j.enggeo.2010.05.016.

[20] FALL M, POKHAREL M. Coupled effects of sulphate and temperature on the strength development of cemented tailings backfills: Portland cement-paste backfill [J]. Cement & Concrete Composites, 2010, 32(10): 819−828. DOI:

10.1016/j.cemconcomp.2010.08.002.

[21] FALL M, BENZAAZOUA M, SAA E G. Mix proportioning of underground cemented tailings backfill [J]. Tunnelling and Underground Space Technology, 2008, 23(1): 80−90. DOI: 10.1016/j.tust.2006.08.005.

[22] CAO Shuai, SONG Wei-dong, YILMAZ E. Influence of structural factors on uniaxial compressive strength of cemented tailings backfill [J]. Construction and Building Materials, 2018, 174: 190−201. DOI: 10.1016/j.conbuildmat. 2018.04.126.

[23] OREJARENA L, FALL M. The use of artificial neural networks to predict the effect of sulphate attack on the strength of cemented paste backfill [J]. Bulletin of Engineering Geology and the Environment, 2010, 69(4): 659−670. DOI: 10.1007/s10064-010-0326-7.

[24] LI Wen-chen, FALL M. Sulphate effect on the early age strength and self-desiccation of cemented paste backfill [J]. Construction and Building Materials, 2016, 106: 296−304. DOI: 10.1016/j.conbuildmat.2015.12.124.

[25] OREJARENA L, FALL M. Mechanical response of a mine composite material to extreme heat [J]. Bulletin of Engineering Geology and the Environment, 2008, 67(3): 387−396. DOI: 10.1007/s10064-008-0148-z.

[26] YILMAZ E, BELEM T, BENZAAZOUA M. Specimen size effect on strength behavior of cemented paste backfills subjected to different placement conditions [J]. Engineering Geology, 2015, 185: 52−62. DOI: 10.1016/j.enggeo.2014. 11.015.

[27] WU Di, DENG Teng-fei, ZHAO Run-kang. A coupled THMC modeling application of cemented coal gangue backfill [J]. Construction and Building Materials, 2018, 158: 326−336. DOI: 10.1016/j.conbuildmat.2017.10.009.

[28] WU Di, HOU Yun-bing, DENG Teng-fei, CHEN Yi-zhou, ZHAO Xiao-long. Thermal, hydraulic and mechanical performances of cemented coal gangue backfill [J]. International Journal of Mineral Processing, 2017, 162: 12−18. DOI: 10.1016/j.minpro.2017.03.001.

[29] XU Wen-bin, HOU Yun-bin, SONG Wei-dong, ZHOU Yi-pei, YIN Tian-jun. Resistivity and thermal infrared precursors associated with cemented backfill mass [J]. Journal of Central South University, 2016, 23(9): 2329−2335. DOI: 10.1007/s11771-016-3291-x.

[30] LIU L, ZHU C, QI C, WANG M, HUAN C, ZHANG B, SONG K I.. Effects of curing time and ice-to-water ratio on performance of cemented paste backfill containing ice slag [J]. Construction and Building Materials, 2019, 228: 116639. DOI: 10.1016/j.conbuildmat.2019.08. 020.

[31] ZHENG Juan-rong, ZHU Ya-lan, ZHAO Zhen-bo. Utilization of limestone powder and water-reducing admixture in cemented paste backfill of coarse copper mine tailings [J]. Construction and Building Materials, 2016, 124: 31−36. DOI: 10.1016/ j.conbuildmat.2016.07.055.

[32] OUATTARA D, BELEM T, MBONIMPA M, YAHIA A. Effect of superplasticizers on the consistency and unconfined compressive strength of cemented paste backfills [J]. Construction and Building Materials, 2018, 181: 59−72. DOI: 10.1016/j.conbuildmat.2018.05.288.

[33] MANGANE M B C, ARGANE R, TRAUCHESSEC R, LECOMTE A, BENZAAZOUA M. Influence of superplasticizers on mechanical properties and workability of cemented paste backfill [J]. Minerals Engineering, 2018, 116: 3−14. DOI: 10.1016/j.mineng.2017. 11.006.

[34] CAO S, YILMAZ E, SONG W, YILMAZ E, XUE G L. Loading rate effect on uniaxial compressive strength behavior and acoustic emission properties of cemented tailings backfill [J]. Construction and Building Materials, 2019, 213: 313−324. DOI: 10.1016/j.conbuildmat.2019. 04.082.

[35] QI Ting-ye, FENG Guo-rui, LI Yan-rong, GUO Yu-xia, GUO Jun, ZHANG Yu-jiang. Effects of fine gangue on strength, resistivity, and microscopic properties of cemented coal gangue backfill for coal mining [J]. Shock and Vibration, 2015, 2015:1−11. DOI: 10.1155/2015/752678.

[36] QI Ting-ye, FENG Guo-rui, ZHANG Yu-jiang, GUO Jun, GUO Yu-xia. Effects of fly ash content on properties of cement paste backfilling [J]. Journal of Residuals Science & Technology, 2015, 12(3): 133−141. DOI: 10.12783/issn. 1544-8053/12/3/3.

[37] CHEN Shao-jie, DU Zhao-wen, ZHANG Zhen, YIN Da-wei, FENG Fan, MA Jun-biao. Effects of red mud additions on gangue-cemented paste backfill properties [J]. Powder Technology, 2020, 367: 833−840. DOI: 10.1016/j.powtec. 2020.03. 055.

[38] CHEN Shao-jie, DU Zhao-wen, ZHANG Zhen, ZHANG Hua-wei, XIA Zhi-guo, FENG Fan. Effects of chloride on the early mechanical properties and microstructure of gangue-cemented paste backfill [J]. Construction and Building Materials, 2020, 235: 117504. DOI: 10.1016/ j.conbuildmat. 2019.117504.

[39] SERVANT S. Détermination des paramètres mécaniques des remblais miniers faits de résidus ciments [D]. Montreal, Quebec: McGill University, 2001.

[40] YILMAZ E, BELEM T, BENZAAZOUA M. Effects of curing and stress conditions on hydromechanical, geotechnical and geochemical properties of cemented paste backfill [J]. Engineering Geology, 2014, 168: 23−37. DOI: 10.1016/j.enggeo.2013.10.024.

[41] YILMAZ E, BENZAAZOUA M, BELEM T, BUSSIÈRE B. Effect of curing under pressure on compressive strength development of cemented paste backfill [J]. Minerals Engineering, 2009, 22(9, 10): 772−785. DOI: 10.1016/ j.mineng.2009.02.002.

[42] YILMAZ E, BELEM T, BUSSIÈRE B, MBONIMPA M, BENZAAZOUA M. Curing time effect on consolidation behaviour of cemented paste backfill containing different cement types and contents [J]. Construction and Building Materials, 2015, 75: 99−111. DOI: 10.1016/j.conbuildmat. 2014.11.008.

[43] GHIRIAN A, FALL M. Strength evolution and deformation behaviour of cemented paste backfill at early ages: Effect of curing stress, filling strategy and drainage [J]. International Journal of Mining Science and Technology, 2016, 26(5): 809−817. DOI: 10.1016/j.ijmst.2016.05.039.

[44] LIU Qiong, WU Wen-xin, XIAO Jian-zhuang, TIAN Yu-ting,

CHEN Jin-yi, SINGH A. Correlation between damage evolution and resistivity reaction of concrete in-filled with graphene nanoplatelets [J]. Construction and Building Materials, 2019, 208: 482−491. DOI: 10.1016/j.conbuildmat. 2019.03.036.

[45] CHU Hong-yan, CHEN Jian-kang. The experimental study on the correlation of resistivity and damage for conductive concrete [J]. Cement & Concrete Composites, 2016, 67: 12−19. DOI: 10.1016/j.cemconcomp.2015.12.005.

[46] HUYNH T P, HWANG C L, LIMONGAN A H. The long-term creep and shrinkage behaviors of green concrete designed for bridge girder using a densified mixture design algorithm [J]. Cement and Concrete Composites, 2018, 87: 79−88. DOI: 10.1016/j.cemconcomp.2017.12.004.

[47] DU Cheng-cheng, LIU Tie-jun, ZOU Du-jian, TENG Jun. Time dependent strain development of early age concrete under step-by-step load history [J]. Construction and Building Materials, 2015, 86: 133−139. DOI: 10.1016/j.conbuildmat.2015.03.116.

[48] BAI Jin-wen, FENG Guo-rui, WANG Ze-hua, WANG Shang-yong, QI Ting-ye, WANG Peng-fei. Experimental investigations on the progressive failure characteristics of a sandwiched coal-rock system under uniaxial compression [J]. Applied Sciences-Basel, 2019, 9(6): 1195. DOI: 10.3390/app90 61195.

[49] RUSATI P K, SONG K I. Magnesium chloride and sulfate attacks on gravel-sand-cement-inorganic binder mixture [J]. Construction and Building Materials, 2018, 187: 565−571. DOI: 10.1016/j.conbuildmat.2018.07.149.

[50] XU Wen-bin, TIAN Xi-chun, QIU Yu, DANG Peng, YIN Tian-jun. Experiment of the resistivity characteristic of cemented backfill mass during the whole consolidation process [J]. Journal of China University of Mining & Technology, 2017, 46(2): 265−272, 344. DOI: 10.13247/j.cnki.jcumt.000648. (in Chinese)

[51] WU Di, ZHANG Yong-liang, LIU Yu-cheng. Mechanical performance and ultrasonic properties of cemented gangue backfill with admixture of fly ash [J]. Ultrasonics, 2016, 64: 89−96. DOI: 10.1016/j.ultras.2015.08.004.

[52] FENG G, DU X, ZHANG Y. 'Optical-acoustic-stress' responses in failure progress of cemented gangue-fly ash backfill material under uniaxial compression [J]. Nondestructive Testing and Evolution, 2019, 34(2): 135−146. DOI: 10.1080/10589759.2019.1576175.

[53] AL-MUFTI R L, FRIED A N. Pulse velocity assessment of early age creep of concrete [J]. Construction and Building Materials, 2016, 121: 622−628. DOI: 10.1016/j.conbuildmat. 2016.06.015.

[54] FARAH M, GRONDIN F, ALAM S Y, LOUKILI A. Experimental approach to investigate creep-damage bilateral effects in concrete at early age [J]. Cement & Concrete Composites, 2019, 96: 128−137. DOI: 10.1016/j.cemconcomp.2018.11. 022.

[55] MEHTA P K, MONTEIRO P J M. Concrete microstructure, properties and materials [M]. Third ed. New York: McGraw-Hill, 2006: 38−41.

[56] MONTEIRO P J M, MASO J C, OLLIVIER J P. The aggregate-mortar interface [J]. Cement and Concrete Research, 1985, 15(6): 953−958. DOI: 10.1016/0008-8846(85)90084-5.

[57] AL-MUFTI R L, FRIED A N. The early age non-destructive testing of concrete made with recycled concrete aggregate [J]. Construction and Building Materials, 2012, 37: 379−386. DOI: 10.1016/j.conbuildmat.2012.07.058.

[58] YIM H J, KIM J H, KWAK H G, KIM J K. Evaluation of internal bleeding in concrete using a self-weight bleeding test [J]. Cement and Concrete Research, 2013, 53: 18−24. DOI: 10.1016/j.cemconres.2013.05.015.

[59] SHOKOUHI P, ZOËGA A, WIGGENHAUSER H. Nondestructive investigation of stress-induced damage in concrete [J]. Advances in Civil Engineering, 2010, 2010(5): 1−9. DOI: 10.1155/2010/740189.

[60] YILMAZ E, BELEM T, BUSSIÈRE B, BENZAAZOUA M. Relationships between microstructural properties and compressive strength of consolidated and unconsolidated cemented paste backfills [J]. Cement and Concrete Composites, 2011, 33(6): 702−715. DOI: 10.1016/j.cemconcomp.2011.03.01349.

[61] WANG Dao-lin, ZHANG Qin-li, CHEN Qiu-song, QI Chong-chong, FENG Yan, XIAO Chong-chun. Temperature variation characteristics in flocculation settlement of tailings and its mechanism [J]. International Journal of Minerals, Metallurgy and Materials, 2020. DOI: https://doi.org/10. 1007/s12613- 020-2022-3

[62] YANG Yi-xuan, ZHAO Tong-qian, JIAO Hua-zhe, WANG Yun-fei, LI Hai-yan. Potential effect of porosity evolution of cemented paste backfill on selective solidification of heavy metal ions [J]. International Journal of Environmental Research and Public Health, 2020, 17(3): 814. DOI: 10.3390/ijerph17030814.

[63] MANSOURI H, AJALLOEIAN R. Mechanical behavior of salt rock under uniaxial compression and creep tests [J]. International Journal of Rock Mechanics and Mining Sciences, 2018, 110: 19−27. DOI: 10.1016/j.ijrmms.2018.07. 006.

[64] DERAEMAEKER A, DUMOULIN C. Embedding ultrasonic transducers in concrete: A lifelong monitoring technology [J]. Construction and Building Materials, 2019, 194: 42−50. DOI: 10.1016/j.conbuildmat.2018.11.013.

(Edited by YANG Hua)

中文导读

分级加载养护对矸石胶结充填柱力学和变形性能的影响

摘要：利用分级加载来模拟采空区矸石胶结充填柱硬化过程中的加载历史。通过电阻率和超声设备监测试件在硬化期间和单轴压缩测试期间的内部损伤。结果表明：1)加压硬化试件 32 d 的单轴抗压强度和弹性模量高于无压力硬化的对照试件，分别为对照试件的 0.5%~20.2%和 7.1%~52.3%，且受初始加载龄期和应力-强度比的影响；硬化期间施加在矸石胶结充填柱上的应力-强度比不应超过 80%。2)初始加载龄期越早，总变形越大，应力-强度比越高，总应变越大；蠕变应变随着应力-强度比的增加而增加，且可以用 Burgers 黏弹性蠕变模型来描述；当应力-强度比小于 80％时，初始加载龄期越早，最后一步加载后的蠕变应变就越小。3)可以根据超声波脉冲速度和电阻率的变化来监测早龄期矸石胶结充填柱在压力下的稳定性。

关键词：矸石胶结充填柱；分级加载养护；抗压强度；弹性模量；变形